An Experimental Investigation of Quadrotor Variations using NASA's Multirotor Test Bed

Sarah Conley
Aerospace Engineer

Carl Russell
Chief, Aeromechanics Office

Dorsa Shirazi
Aerospace Engineer

Kristen Kallstrom
Aerospace Engineer

Carlos Pereyra
Aerospace Engineer

Stephen Wright
Aerospace Engineer

NASA Ames Research Center
Moffett Field, CA, 94035, USA

ABSTRACT

Generating multiple high-quality sets of rotor performance data is necessary to validate Vertical Take-Off and Landing (VTOL) aircraft performance prediction codes across a broad range of vehicle configurations. Many aircraft companies are actively pursuing multirotor vehicle configurations, which has created a need for validation data for multirotor systems. The NASA Multirotor Test Bed was designed to accommodate a broad range of reconfigurable multirotor systems and to measure rotor performance and loads in a wind tunnel environment. This paper presents results from the second wind tunnel entry of the test bed, which was completed in August 2022. This wind tunnel test focused on a quadrotor configuration, with variations in rotor placement, blade number, and rotor phasing, across a range of wind tunnel test conditions. This paper describes the test methods and provides and discusses a sample of the quasi-steady and dynamic loads data that were collected during the test program.

NOTATION

$\hat{C}$	resultant calibration matrix coefficients
C_T	thrust coefficient
C_T/σ	blade loading
dz	vertical difference between front and back rotors [in]
$\widehat{F}$	approximated loading force [lb]
F_x	force reading from load cell in x-direction [lb]
F_y	force reading from load cell in y-direction [lb]
F_z	thrust force reading from load cell [lb]
M_x	roll moment reading from load cell [in-lb]
M_y	pitch moment reading from load cell [in-lb]
M_z	torque reading from load cell [in-lb]
N	number of blades
p	number of multivariate parameters
P_i	induced power [lb-ft/s]
P_o	profile power [lb-ft/s]
q	dynamic pressure [psf]
R	radius of the rotor blade [in]
t	distribution used for confidence interval calculations
$u_{pi,95}$	uncertainty, 95% of predictive interval
u_{tot}	total uncertainty
V	voltage [V]
v_0	input voltage [V]
VTOL	Vertical Take-Off and Landing
σ	blade solidity
σ_i	variance term

INTRODUCTION

High-quality test data are a critical component to the development and validation of software tools used for Vertical Take-Off and Landing (VTOL) rotor performance predictions. These data are needed for tools at varying levels of fidelity, from simple prediction tools up through time-accurate high-fidelity Computational Fluid Dynamics (CFD) simulations. Up until around the last decade, wind tunnel testing for VTOL rotor systems focused almost entirely on single main rotor, tandem, or tiltrotor configurations. With the development of the electric VTOL market over the past several years, the design space for VTOL rotor configurations has expanded significantly, especially in the Urban Air Mobility (UAM) domain. Correspondingly, there is now a need for validation data to support simulations of these new rotor configurations.

The Multirotor Test Bed (MTB) was developed for the purpose of testing a wide range of multirotor systems on a single test platform. The development of the MTB hardware was first described in [Ref. 1], and the first wind tunnel test of the MTB, referred to as MTB1, was completed in the U.S. Army 7- by 10-Foot Wind Tunnel at NASA Ames Research Center in 2019 [Ref. 2]. The MTB test rig allows for flexible placement of up to six rotors with diameters up to about 24 inches, with full capabilities of the MTB described in [Refs.

Presented at the Vertical Flight Society's 81st Annual Forum & Technology Display, Virginia Beach, VA, USA, May 20-22, 2025.

1,2]. In addition to allowing for variations in rotor placement, the pitch angle of the entire rig is adjustable, and each rotor has its own tilt actuator that allows for independent variation of the rotor tilt angle. Additional details are provided in later sections. The primary measurements collected by the MTB are the quasi-steady and dynamic rotor loads. These loads are collected by six-axis load cells located under each rotor. The MTB in its test configuration for the second wind tunnel test (MTB2) described here is shown in Figure 1. The following subsections provide brief descriptions of the MTB1, MTB2, and the upcoming MTB3 test.

Multirotor Test Bed Entry 1

The first wind tunnel test of the MTB (MTB1) served as a shakedown test of the new test rig, with a wide-ranging test matrix that was mainly intended to exercise all the different mechanical and measurement hardware systems. Data collected during that test have already been used for validation studies for various simulation tools including RotCFD [Ref. 3], CHARM [Ref. 4], CAMRAD II [Refs. 5,6], and OVERFLOW [Ref. 7]. The rotor used for the MTB1 test was an off-the-shelf KDE-CF245-DP with 24.5-inch diameter. The MTB had the ability to adjust rotor RPM, rotor tilt, full rig pitch, and number of rotors.

Multirotor Test Bed Entry 2

The second wind tunnel test entry of the MTB (MTB2) was completed in August 2022, in the same facility, the U.S. Army 7- by 10-Foot Wind Tunnel, with the test configuration shown in Figure 1. MTB2 was intended to focus on a scaled-down version of the NASA Revolution Vertical Lift Technology (RVLT) Project concept quadrotor vehicle configuration [Ref. 3] with variable height of the back rotors to investigate effects of rotor-rotor interference. The RVLT concept quadrotor is one of several concept vehicles that were developed by the RVLT Project to focus research on a set of objective aircraft that are realistic, non-proprietary representations of the broad range of eVTOL aircraft currently under development. The different RVLT concept vehicles are described in References 8 and 9. In the MTB2 test entry, the MTB was tested in three quadrotor configurations of varying vertical separation between the front and back rotors, denoted as dz/R, including dz/R=0, 0.33, and 0.57. Note that dz/R=0.33 represents the rotor separation of the RVLT concept quadrotor. In addition to the variable rotor heights, the MTB2 test included the ability to control the azimuthal phase angle between rotors. Rotor phase angle control has been proposed by various researchers as a method to improve overall vehicle performance and to reduce noise and vibrations [Ref. 10]. The main structural hardware modification for this test was the installation of new, more robust actuators that had negligible backlash. Additionally, the rotors, discussed more thoroughly in later sections, were custom designed to facilitate public distribution of the rotor geometry.

Multirotor Test Bed Entry 3

Additional MTB tests are planned for the future, one of which will focus on the evaluation of noise produced by multirotor systems at model- and full-scale. The third MTB wind tunnel test entry (MTB3) is planned to take place in the National Full-Scale Aerodynamics Complex (NFAC) at NASA Ames in 2026 and will provide the ability to measure noise in an anechoic facility. MTB3 will have previous model capabilities and a new hub with ground adjustable collective. The blades used in MTB2 will be tested along with new blades, both with 24.5-inch diameter. Future testing after MTB3 will focus on a larger multirotor system that will provide research data on the effects of rotor size scaling.

Prior MTB Publications

There have been several prior publications on the MTB, listed in the references section and above, but this is the first publication that presents the corrected wind tunnel test data from the MTB2 wind tunnel test. References 1 and 11 cover the design and loads and stress analysis of the MTB. Reference 2 gives a description of the MTB1 test and presents some of the data. This paper will present a selection of the data from MTB2 with updated calibrated load cell matrices. Another paper presented at this venue, Reference 12, presents comparisons of the MTB2 data to CHARM and OVERFLOW simulation results, identifying best practices for the simulation tools and identifying suggestions for the future MTB wind tunnel tests. There will be some overlap between the experimental data presented in this paper and those presented in Reference 12. However, this paper will present more experimental data, go into greater detail regarding the trends in the experimental data, and will not be comparing the data to results from simulation tools. The MTB2 data report, Reference 13, has a more detailed overview of the test and lists all the data tables. The data report only shows a few plots and focuses mainly on the test setup, execution, data tables, etc., and does not draw any conclusions from the data. However, this paper presents several plots, identifies some trends in the data, and aims to interpret the results.

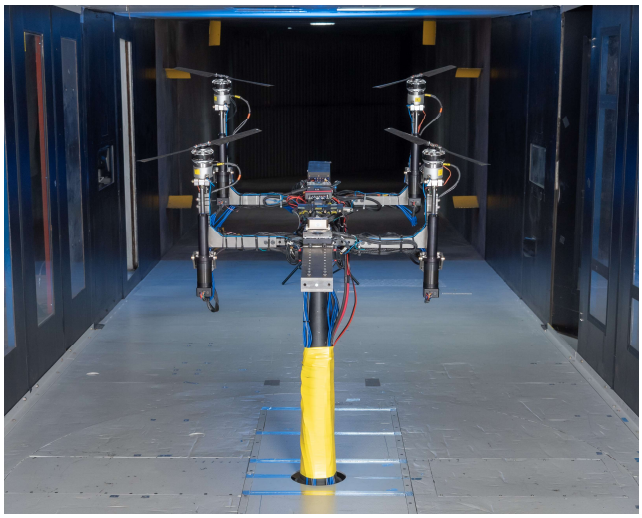

Figure 1: Front view of the MTB2 in the U.S. Army 7- by 10-Foot Wind Tunnel.

TEST DESCRIPTION

U.S. Army 7- by 10-Foot Wind Tunnel

Like the first MTB test, the 2022 test (MTB2) described in this paper was carried out in the U.S. Army 7- by 10-Foot Wind Tunnel at NASA Ames Research Center. This is a closed-throat, single-return wind tunnel with a 14:1 contraction ratio, and a test section of 7.0 x 10.0 x 15.0 feet. The MTB was mounted on a strut and secured to the turntable in the center of the test section. The cabling was routed underneath the tunnel floor through the opening at the strut (secured to the strut with the yellow tape in Figure 2) and was either routed directly below the turntable or through the floor to the control room. Also shown in Figure 2 is the skylight on the ceiling of the test section, above which a strobe light and camera were placed, which allowed for verification of the rotor phase angle. Additional details regarding the wind tunnel can be found in the data report, Reference 13.

Figure 2: Test section ceiling and test crew working on model.

For the MTB2 test, operations typically involved five people: Tunnel Operator, Test Engineer/Director, Safety-of-Flight (SOF) Monitor, Model Operator, and Data Operator. The control room setup is shown in Figure 3. All functions of the model and the tunnel were controlled from within the control room, and test section conditions and video of the model were displayed on the large monitors at the front of the room.

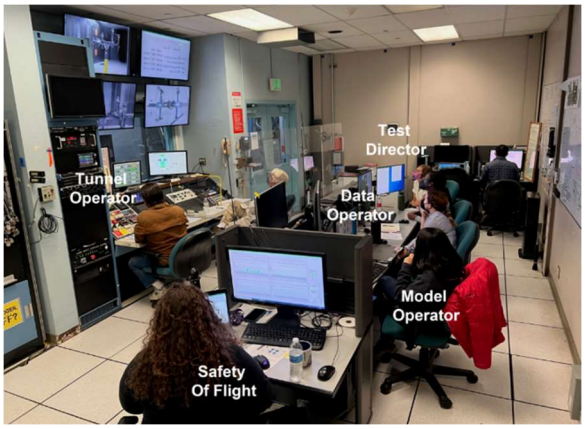

Figure 3: 7- by 10-Foot Wind Tunnel control room with MTB2 operator positions identified.

Test Matrix

For the quadrotor layout tested here, there were three primary rotor configuration variables that were studied – vertical spacing, phasing, and solidity – in addition to the typical variables of dynamic pressure (wind speed), rotor rotation rate, model pitch angle, and rotor tilt angle. These variations were chosen based on results from previous computational studies indicating a need for additional validation data. Descriptions of each of the rotor variations, along with the computational studies that inspired each experimental investigation are given below:

1) *Rotor vertical spacing study:*
   The height difference of the back rotors to the front rotors expressed as a function of rotor radius, dz/R, was tested at three different values: dz/R=0, 0.33 and 0.57 (the concept quadrotor has a dz/R=0.33). The effects of dz/R on rotor performance were studied in-depth through OVERFLOW simulations in Reference 14.
2) *Rotor azimuthal phasing study:*
   The relative phase angle of the rotors was varied from 0 to –90 deg, using a custom electronic speed controller built by Launchpoint Electric Propulsion Solutions that allowed for on-the-fly adjustment of the phase angle. The effects of rotor phasing on vehicle vibratory loads are particularly of interest and have been studied with the RMAC comprehensive analysis code in Reference 10.
3) *Rotor solidity study:*
   Three different rotor hubs were used for testing, allowing for 2-, 3-, and 6-bladed versions of the rotor with identical blades. Rotor solidity has long been a design variable in rotorcraft sizing studies and was recently explored in Reference 15, which looked at multiple iterations of the RVLT Concept Vehicles.

As can be seen from Table 1, the test matrix is quite extensive and there are multiple test variables that allow a plethora of testing configurations. This table is a condensed version of the MTB2 Test Matrix and is not all-encompassing. For the complete MTB2 Test Matrix, see the MTB2 data report [Ref. 13]. For brevity, not all testing conditions are discussed and shown in this paper.

Table 1. Condensed MTB2 test matrix.

dz/R	0.33	0.00	0.57
Phase [deg]	0, –30, –60, –90	0, –90	0, –90
# blades	2, 3[a], 6[a]	2	2
# rotors	1, 2[b], 2[c], 4	1, 2[c], 4	1, 2[c], 4
Tilt [deg]	0, –3	0, –3	0
Conditions for all dz/R configurations			
q [psf]	0, 0.48, 1.90		
Pitch [deg]	0, –1, –3, –5, –10		
RPM	2000, 2500, 3000		

Notes:
[a] Not all 3- and 6-bladed runs were performed for all testing conditions for the dz/R=0.33 configuration given in this table; [b] Side-by-side; [c] Tandem.

Coordinate Systems

Figure 4 shows the Balance Coordinate System and the Hub Coordinate System. These axes are identical to each other except that they are displaced a distance of "HUB_DIST" along the z axis (2.783 inches). This is the distance from the moment center of the Balance Coordinate System, the top of the load cell, to the center of the hub in the rotor plane. The Hub axes are defined as follows:

Fx_H downstream
Fy_H toward control room
Fz_H up
Mx_H positive roll left
My_H positive pitch up
Mz_H positive torque CCW (as viewed from above)

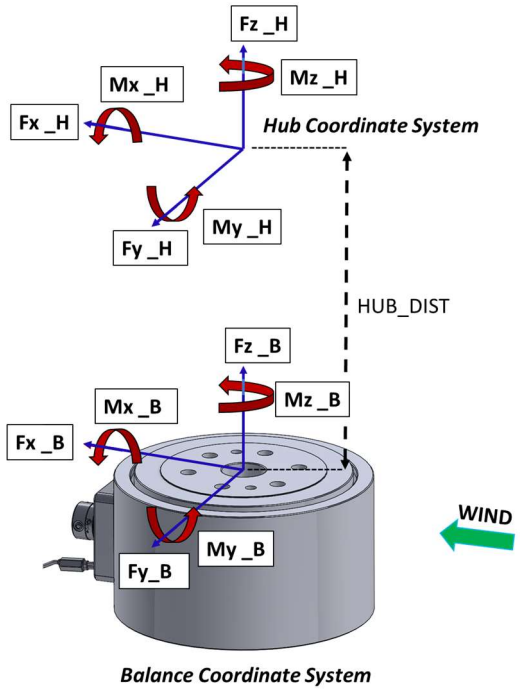

Figure 4: The load cell forces and moments in the Balance and Hub Coordinate Systems.

Note that this coordinate system obeys the right-hand rule and may differ from other reported wind tunnel experimental or flight data.

Hardware

The MTB was designed to be an extremely versatile and reconfigurable system. It can have up to 6 rotors, though for this test only up to 4 were tested, and the rotors can be repositioned along the x, y, and z axes with individual tilt rotation available via the linear actuators. Figure 5 provides a CAD image of the MTB in the quadrotor configuration, with the rotor numbers labeled. Table 2 provides a list of the capabilities and range of the test stand as it was during the MTB2 Test Campaign.

A stepper motor under the main strut turns a jack screw inside, moving a lug on the strut up and down. There is a linkage connecting that lug to the strongback (the backbone of the MTB) which allows the full rig to pitch up and down.

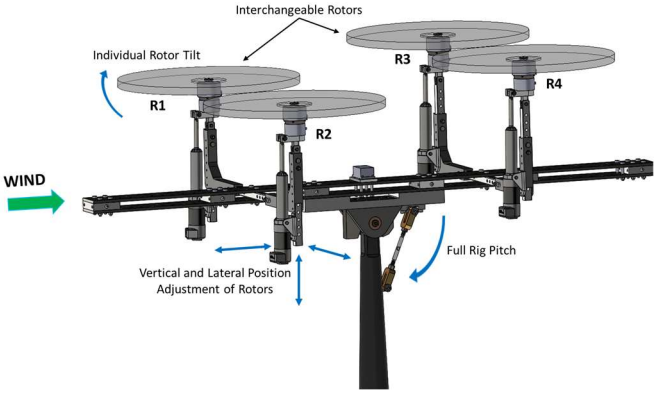

Figure 5: CAD image of the MTB2, isometric view.

Table 2: MTB2 capabilities and limits.

Characteristic	Range
Rotor diameter	24.5 inches (same as the KDE-CF245-DP rotors of MTB1)
Max. rotor RPM	4,500
Lateral spacing	24.7–38.7 inches, adjustable in 1-inch increments (2-inch increments if symmetric about the centerline)
Longitudinal spacing	25.5–72 inches, adjustable in 1.5-inch increments
Vertical position	9 inches of travel, adjustable in 1-inch increments
Individual rotor tilt	–90 deg forward to 5 deg aft, adjustable in arbitrary increments
Full MTB pitch	–30 deg forward to 10 deg aft, adjustable in arbitrary increments
Max. wind speed	40 ft/s, higher if vibratory load limit is not reached

While the configuration of the MTB is easily reconfigurable, the system was designed with very rigid materials (high strength stainless steel) which both increased safety factors and decreased structural deflection in the strongback, lateral support beams, and vertical support beams that hold the rotor stacks. The MTB was designed to minimize deflections, keeping the total angular displacement of the rotors less than 0.1 deg in any direction with reference to the ground for all planned test conditions. To be approved for the wind tunnel, a minimum safety factor of 3 on yield strength and 4 on ultimate strength is required. A blade out analysis was performed, and all parts showed a minimum safety factor of 1 on yield for blade out conditions. For more details about the design and the loads and stress analysis of the MTB, see Reference 11.

Blade Geometry

The MTB2 test incorporated non-proprietary, custom designed rotor blades. Some characteristics of the MTB1 rotor blades were retained, primarily the blade radius and the rotor solidity. The MTB2 blade has a constant chord with the Eppler 387 (E387) airfoil – chosen for its performance characteristics at low Reynolds numbers [Ref. 1616].

A design study was performed in the CAMRAD II rotorcraft comprehensive analysis code [Ref. 55], to determine desired settings for the blade's linear twist distribution and built-in collective pitch. Assessments of two performance metrics, power defined as profile power (P_o) + induced power (P_i), and blade loading (C_T/σ), were used to determine the desired values for twist and built-in collective pitch. A linear twist sweep was simulated in CAMRAD II with C_T/σ trimmed to 0.09 (a chosen design point matching the concept quadrotor). Simulations were run for 40 ft/s, 2000 RPM, and for –5 and –10 deg rotor tilt, operating conditions which were deemed representative of the eventual wind tunnel test conditions. Figure 6 shows the results of the twist sweep with 2000 RPM, 40 ft/s, and –10 deg rotor tilt. The optimum twist, -16 deg (the red line in the figure), and the corresponding built-in collective, 6.7 deg, were selected for the blade. The overall MTB2 blade geometry is detailed in Table 3.

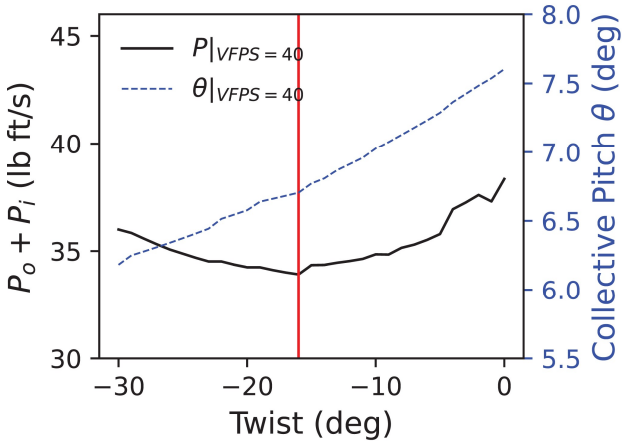

Figure 6: Power and collective pitch vs twist, wind speed=40 ft/s, rotor tilt= –10 deg.

Table 3: MTB2 as-built (APC modified) blade geometry.

Property	Value
Root cutout, %R	0.22
Rotor radius	12.245 inches
Chord length	1.54 inches
Airfoil	Eppler 387
Blade twist	–16 deg, linear from root to tip
Built-in collective pitch	6.7 deg at 75% radius
Trailing edge thickness	~0.020 inches *Sharp corners at tip rounded to radius of 0.020 in*

Ultimately, due to manufacturing constraints, some modifications to the airfoil geometry (such as thickening the trailing edge) were required by the manufacturer, Advanced Precision Composites (APC).

Testing Procedure

The intent of the MTB2 test was to measure steady and vibratory forces and moments as a function of dynamic pressure (wind speed), attitude, MTB configuration, rotor phase, and rotor RPM. The general strategy for testing was to vary RPM for a given combination of dynamic pressure (tunnel speed), model pitch angle, rotor phase, and configuration. The model pitch was then changed, and RPM was varied again for multiple rotor tilt angles. Depending on how long a pitch and RPM sweep took at a given wind speed, multiple wind speeds could be tested in a single test run. Because the tunnel operator and test director set on a dynamic pressure of 0.48 psf and 1.90 psf +/- 0.02 psf, some of the wind tunnel speed values may deviate more from 20 ft/s and 40 ft/s. Setting on dynamic pressure allows for better comparison of the data since it takes the humidity and air temperature into account.

Aerodynamic and weight tares were performed throughout the test campaign and were used for postprocessing of the data. R-Cals were performed at the beginning and ending of each run to verify the health of the load cells. Repeat points were taken at the beginning and end of each run to help account for any hysteresis or load cell offsets caused by temperature fluctuations. These were referred to as "housekeeping wind off" and "housekeeping wind on" points and were taken at 2000 RPM, 0 pitch, 0 tilt, and wind tunnel speed of either 0 or 20 ft/s (~0.48 psf dynamic pressure).

Data Collection and Instrumentation

Both quasi-steady and dynamic data were recorded for the load cells for this test. The quasi-steady data were mean values from unfiltered dynamic channel measurements. The dynamic data were recorded following the quasi-steady point and represent a time history of the loads sampled over 5 seconds. Data were recorded and stored in multiple files with low-speed channels (tunnel parameters) sampled at 10 Hz and

high-speed channels (load cells and accelerometers) at 4 kHz. All load cell data underwent zero subtraction and temperature corrections, detailed in the post-processing section. The primary data acquisition used for this test was a LabVIEW-based interface called the Standard Data Acquisition System (SDAS). The SDAS uses a flexible architecture to acquire data for several channels. The various instruments used for this test are summarized below.

Load Cells: The primary data of interest for this test were quasi-steady and dynamic loads, which were measured using Interface model 6AR70A-S11 six-axis load cells. The six channels from each load cell were routed to a junction box, where the signal was amplified and filtered with a 1 kHz low-pass filter. The signal was stored in both engineering units and raw voltages. The signal was also sent to Safety of Flight for loads monitoring during testing. The excitation at the load cell was adjusted to match the calibration excitation, and then an R-Cal was taken at the beginning and end of each run to monitor the health of the gauges.

RPM Sensors: The RPM was measured using a 1/rev Hall sensor which was mounted under the motor, sending signals to the control system and data storage for both real-time and recorded RPM values.

Thermocouples: Temperatures of the load cells and power bus were measured using thermocouples. The thermocouple signals were sent unamplified to the MTB Control System Data Acquisition System where they were filtered and averaged. They were then sent to the SDAS via an RS-232 line. Due to the lack of amplification, the thermocouple signals were very noisy while the motors were running, so only the starting and ending temperature measurements proved to be useful.

Accelerometers: Tri-axial 5g accelerometers were used to measure acceleration of the load cell mounting plate. The signals were transmitted to an amplifier, filtered, and then recorded directly in the dynamic raw storage without zero-subtraction.

Inclinometer: An analog inclinometer was used to measure the pitch angle of the MTB strongback. The inclinometer was calibrated in-place, with a linear conversion for signal processing.

Rotor Tilt: Rotor tilt was controlled indirectly by an analog voltage sent to the linear actuators for the different rotors. There was an in-place calibration performed for each actuator to determine a polynomial conversion of actuator analog input to rotor tilt.

The additional details of MTB2 data collection can be found in the Multirotor Test Bed Wind Tunnel Test data report [Ref. 13].

Post-Processing and Data Correction

Each load cell was calibrated post-test to determine a more accurate model for calculating forces and moments from the load cell readings. Additionally, the post-test calibration data was used to establish an understanding of the uncertainty quantification in the load cell response. A pool of post-test calibration data was gathered from a sequence of known loading cases, in which the loads and moments were applied in both positive and negative directions up to a maximum of 50 lb (resulting in 142 in-lb moments) in combined loading cases and 120 in-lb in the pure moment cases. These data were gathered in discrete intervals of 5 lb and applied in triangular loading / unloading schedules. This cycle was repeated three times, providing ample data for cross-validation.

The calibration data were partitioned into a training set and a validation set, using an 80% and 20% ratio respectively. A weighted least squares model was used to determine the optimal multi-dimensional linear set of conversion coefficients[†] (the 6x6 conversion matrix), whereby its performance was quantified by residual variance on the testing set. Note, upon inspection of the load cell channel responses per each loading configuration, it was determined that channels were interdependent. This is reflected in the fact that the linear calibration matrices are not strongly diagonal. The variance is impacted from coupling of the load cell gage signals. The uncertainty quantification is discussed in the next section.

Before converting the raw voltages into engineering units, the data was first tared or zero-subtracted from its baseline point. The zero or baseline points were taken at the beginning of each run. This took out any initial load on the model. After the raw voltages were tared, they were converted into engineering units via the calibrated model. These were the initial load values. Then a series of post-processing steps were taken to account for load cell drift (skewness), aerodynamic drag, inertial loading of the motor, and weight influences. At the start and end of each run static points were taken, in which no load was applied (all testing parameters set to zero). These points, called static points, served as measures of bias and linear drift through comparing the beginning and ending static points for each run. Aerodynamic and weight tares were recorded in the tunnel during the test entry and were applied to the data to remove their effects. The process of implementing the data corrections is further explained in the data report [Ref. 13].

[†] Optimal in the sense that the chi-squared distribution is minimized for the linear set of dimensions.

Uncertainty

This section explains how the variances (denoted by σ_i) and the total uncertainty values (u_{tot}), shown as error bars in the plots, were calculated. The error distribution of the load cell responses depends highly on the nominal load values and the load configuration. This error is assumed to be normally distributed. Placing an interval of upper and lower bounds on the mean loads can be computed by the 95% predictive interval, $u_{pi,95\%}$. The equation to calculate the 95% predictive interval, is shown below.

$$u_{pi,95\%} = \pm t_{n-p,0.975}\sigma_i\sqrt{1 + v_0^T(V^TV)^{-1}v_0} \qquad (1)$$

Given some input voltage v_o taken during experimentation, the possible regions of load values may be heuristically determined from Equation 1. Here, $t_{n-p,0.975} \approx 1.96$ represents the 95% quantile of the t-distribution. Two key pieces of information saved from calibration are the variances σ_i, and the covariance $(V^TV)^{-1}$ of the calibration voltage readings. These values are then used to determine the upper and lower bounds of the mean load predictions. The variances shown in Table 4 are used in Equation 1 and are a measure of the mean deviation between applied and model predicted loads across all load schedules.

Table 4: MTB2 Load Cell Variances.

Load Cell	σ_{Fx} (lb)	σ_{Fy} (lb)	σ_{Fz} (lb)	σ_{Mx} (in-lb)	σ_{My} (in-lb)	σ_{Mz} (in-lb)
LC1	0.93	0.19	0.32	0.65	0.82	0.64
LC2	0.08	0.04	0.29	0.14	0.31	0.56
LC3	0.37	0.21	0.08	0.16	0.13	0.08
LC4	0.09	0.08	0.07	0.29	0.22	0.11

As seen in Table 4, it is observed for load cells 1 and 2 that variance in the thrust directions is nominally higher than in load cells 3 and 4 and thus may yield higher regions of predictive intervals (larger error bars). While higher order models were investigated with the hopes of reducing co-linearity (between load cell channels) and consequentially reducing variance, the mean load predictions were quite similar to the linear model used. The uncertainty was also calculated for the nonlinear, higher order model but yielded very similar values for thrust and torque. Since the linear model had been more thoroughly examined and reviewed, it was decided to remain with the linear model. Equation 2 calculates the total uncertainty for a specific load in a particular configuration by combining the uncertainty from the predictive interval with the mean dynamic uncertainty.

$$u_{tot} = \sqrt{{u_{pi,95\%}}^2 + {u_{dyn}}^2} \qquad (2)$$

Finally, incorporating u_{tot} into Equation 3 gives the upper and lower error bounds on the loads and is what is shown in the error bars on the plots.

$$\hat{F} = V\hat{C} \pm u_{tot}(V) \qquad (3)$$

where $\hat{F}$ is the (approximated) loading force yielded by the linear model terms $V\hat{C}$ (voltage times the 6x6 matrix coefficients) bounded by the total uncertainty. Since the uncertainty depends on a specific load value, the equation is expressed as a function of voltage, V.

RESULTS AND ANALYSIS

This section presents a subset of the results from the MTB2 test. The objective of this section is to demonstrate the types of results that can be analyzed from the data and to discuss possible discrepancies in the data collection abilities. The individual quasi-steady rotor loads and uncertainty studies will be presented and discussed first, followed by the multirotor quasi-steady loads, and ending with the dynamic loads.

Individual Rotor Quasi-Steady Loads and Uncertainty Studies

First, the individual rotor thrust and torque values are analyzed to help determine potential differences in the measurements between rotors and load cells. Theoretically, each individually tested rotor should yield the same forces and moments for each test condition, and any observed differences between the loading values could be due to load cell differences, rotor geometry differences, and/or test stand interference. Note that the dynamic pressure (q) 0.48 psf and 1.90 psf is equivalent to about 20 ft/s and 40 ft/s, respectively. In the data, the q values can vary +/- 0.02 psf. Rotor 1 is denoted by R1, and the other rotors are denoted similarly. In the force and moment plots, the back rotors are denoted with a dashed line. Additionally, the error bars shown in the plots represent the uncertainty in the measurements. The method for obtaining the error bars is described in previous sections. Figure 7 shows the rotation direction and position of the rotors in the quadrotor configuration for the rotors phased with 0 deg separation. The blue line represents blade 1. Rotors 2 and 3 were phased with respect to rotors 1 and 4. The rotors were not phased for the single rotor runs.

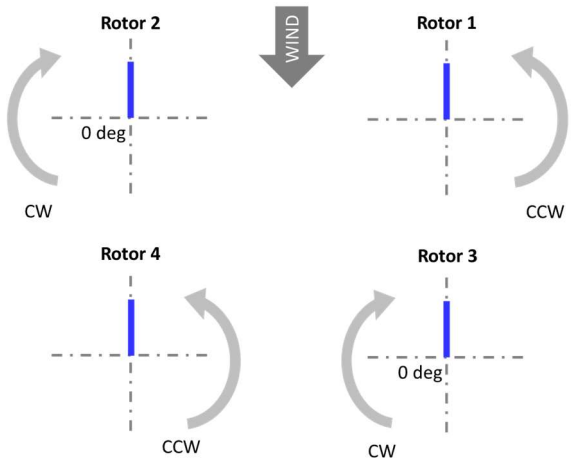

Figure 7: Schematic of rotors phased with 0 deg separation.

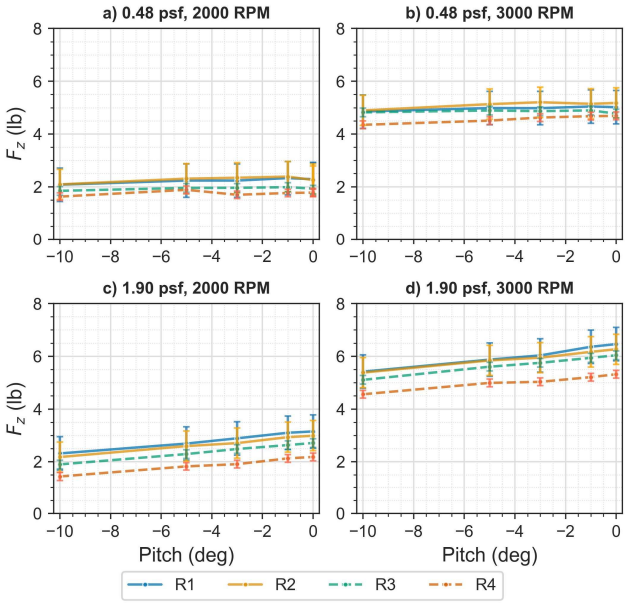

Figure 8: Individual rotor runs, thrust values for different dynamic pressures and rotor speeds as a function of pitch angle, with *dz/R*=0.33 and tilt=0 deg.

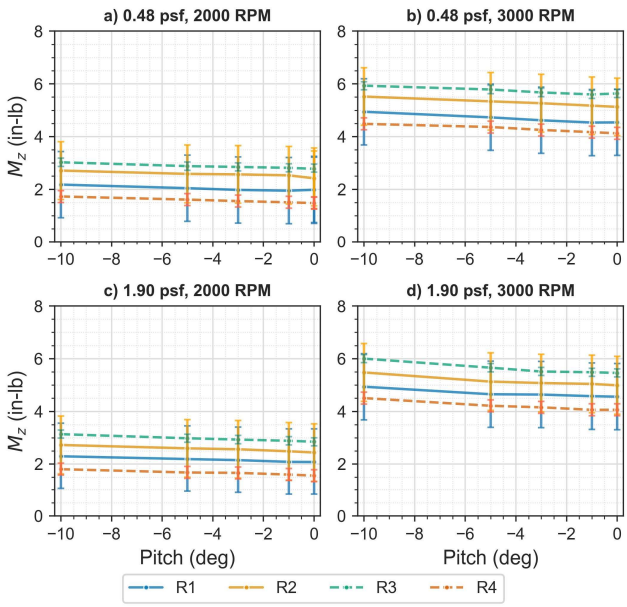

Figure 9: Individual rotor runs, torque values for different dynamic pressures and rotor speeds as a function of pitch angle, with *dz/R*=0.33 and tilt=0 deg.

Figure 8 presents thrust from the single rotor runs at different tunnel speeds and RPMs. R1 and R2 show very similar thrust values at all conditions with R2 thrust being slightly higher than R1 thrust at lower tunnel speeds and the opposite being true for higher tunnel speeds. The thrust from R3 is below that of R1 and R2, with the difference between them increasing with higher tunnel speeds and lower RPM. The thrust from R4 is the lowest of all, with the difference to the other rotors increasing with increasing tunnel speed and increasing RPM. When looking at the data from multirotor runs, it is important to note that R4 may be reading slightly lower thrust values than the other rotors not because of an aerodynamic phenomenon, but because of a potential difference in load cell measuring capability or rotor geometry. Overall, all the rotors showed that higher tunnel speeds resulted in a greater dependency of thrust on pitch, with thrust increasing as the pitch approached 0 deg.

Figure 9 shows torque vs pitch for the same conditions as in Figure 8. The clockwise rotating rotors, R2 and R3, showed much higher torque than the counter-clockwise rotating rotors, R1 and R4, for all conditions. From the previous figure, it is shown that R3 and R4 yielded less thrust, so it would make sense for R4 to have lower torque, but R3 having higher torque with lower thrust suggests that there could be an inefficiency present – potentially a less efficient motor, friction in the motor bearings, less efficient blades, etc. The beginning and ending load cell temperatures for several runs were checked, and the load cell temperatures were all within about 1 deg of each other.

As mentioned before, R-Cals were performed on the load cells at the beginning and ending of each run, to assess the health of the sensors. Because the R-Cals always passed their checks, it is unlikely that the load cells were misused. Again, when looking at the data from multirotor runs, the discrepancy between the CW and CCW torques should be considered. It should be noted that the conditions in Figures Figure 8 and Figure 9 were also checked for a tilt value of –3 deg. The resulting plots showed that tilting had very little impact on the thrust and torque, and thus those plots were excluded from this paper for brevity.

Figures Figure 10 and Figure 11 show an uncertainty study with R1 and R4 and load cells 1 and 4 (LC1 and LC4) for thrust and torque, at different tunnel speeds and rotor RPMs. Three different cases are compared to each other: rotor 1 on load cell 1 (R1 on LC1), rotor 4 on load cell 4 (R4 on LC4), and rotor 4 on load cell 1 (R4 on LC1). For the last case, R4 on LC1, the hub that was in position 4 (back port) replaced the hub in position 1 (front starboard). The figures show that the thrust of R1 on LC1 was very similar to the thrust of R4 on LC1, with R4 on LC1 being slightly lower. This could be due to a slight deviation in rotor geometry between R1 and R4. This difference in thrust decreased with increased tunnel speed but increased with increased RPM. More notably, the thrust of R4 on LC4 was significantly lower than the thrusts of R1 on LC1 and of R4 on LC1. This indicates that LC4 was reading lower thrust values for the same condition with the same rotor. This could be due to the load cell measuring capability, or the wake being influenced by the test stand. It is unlikely that these differences could be due to tunnel flow quality since a flow quality study was done a few years prior in 2019 [Ref. 17] and yielded very uniform readings.

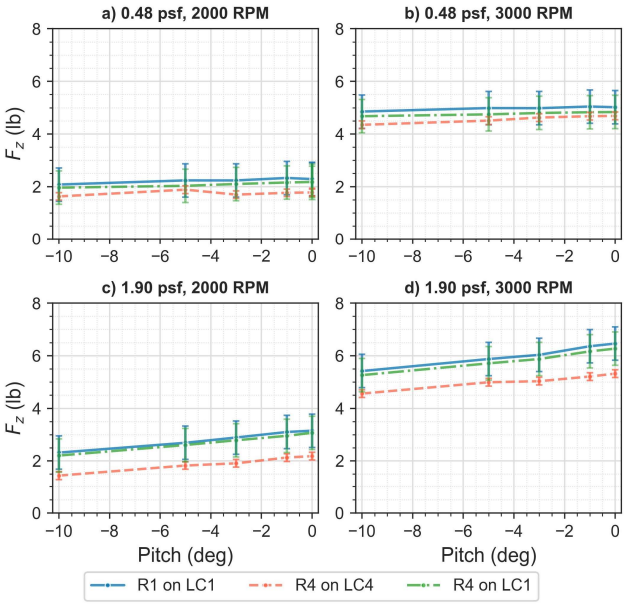

Figure 10: Thrust uncertainty study between R1 and R4 and LC1 and LC4 as a function of pitch angle, *dz/R*=0.33 and tilt=0 deg.

Similar observations can be made for the torque values presented in Figure 11. R4 on LC4 yields the lowest torque value, with R4 on LC1 coming in second, and R1 on LC1 being the highest. The differences in torque values between the three curves are much smaller than those for the thrust values in Figure 10. R4 on LC1 torque is closer to R1 on LC1 for lower RPMs and is in the middle of the two curves for higher RPMs. Increasing tunnel speed did not show much effect on the differences between the curves. Additional uncertainty studies are planned for future MTB tests to facilitate identifying sources of error.

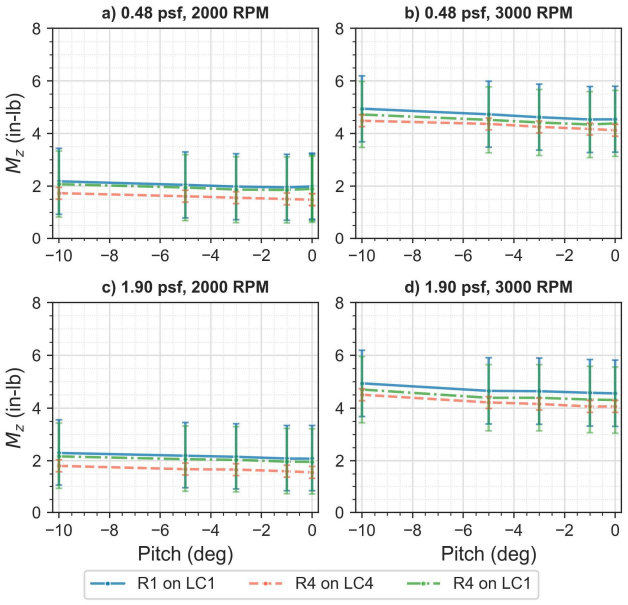

Figure 11: Torque uncertainty study between R1 and R4 and L1 and L4 as a function of pitch angle, *dz/R*=0.33 and tilt=0 deg.

When observing the data, it should also be taken into consideration that the error bars for R1 and R2 are higher than those for R3 and R4. This is due to the variance of the individual load cells and is explained in the Uncertainty Section.

Multirotor Quasi-Steady Loads

In this section, several multirotor studies are presented. The figure captions for each study state which configuration is being observed: quadrotor, side-by-side, or tandem; *dz/R*=0, 0.33, or 0.57. Recall that the *dz/R*=0.33 condition is the RVLT concept quadrotor configuration and the dynamic pressure (q) 0.48 psf and 1.90 psf is equivalent to about 20 ft/s and 40 ft/s, respectively. The studies were done with two-bladed rotors with rotors in phase with 0 deg separation unless otherwise stated. For the quadrotor runs, often only the starboard rotors are shown for brevity.

During testing, several runs were performed with 2-, 3-, and 6-bladed rotors. Figure 12 shows some results from that quadrotor solidity study. The subplots show the blade loading on each individual rotor. Blade loading is the highest for the 2-bladed rotors across all rotors. The front rotors show higher blade loading than the back rotors for all solidities.

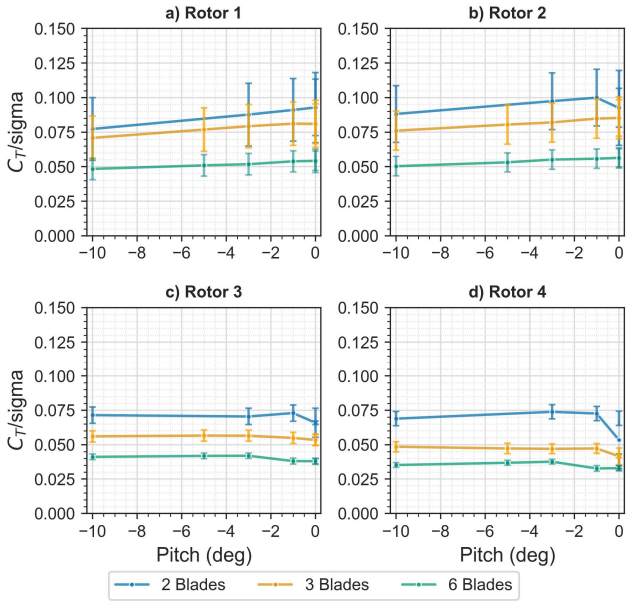

Figure 12: Blade loading vs pitch for different quadrotor solidities for *dz/R*=0.33, q=0.48 psf, RPM=2000, and tilt=0 deg.

Figure 13 shows the effect of tilt on thrust and torque for the starboard rotors, R1 and R3, in the *dz/R*=0.33 configuration for different tunnel speeds and RPMs as a function of vehicle pitch. Only the starboard rotors are shown, and as expected, the front rotors show higher thrust than the back rotors. Consistent with the results discussed in the previous section, R3 shows higher torque than R1. The difference in thrust with tilt is more noticeable at higher tunnel speeds, Figure 13 (b), for R1 and for R3 between pitch of –3 and 0 deg, with the –3

deg tilt yielding lower thrust values. All the other subplots show that tilt does not have a large effect on thrust and torque. In Figure 13(d), the torque tends to increase slightly for tilt of –3 deg for both rotors between pitch of –3 and 0 deg.

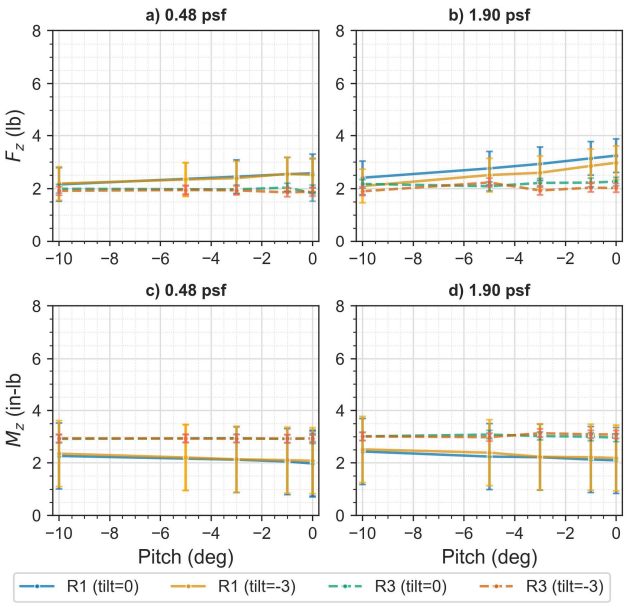

Figure 13: Starboard rotors tilt comparison for thrust and torque for the quadrotor configuration at *dz/R*=0.33, *q*=0.48 and 1.90 psf, and RPM=2000.

Figure 14 shows the impact of *dz/R* on R1 and R3 in the quadrotor configuration for various RPMs and the lower tunnel speed of 0.48 psf. Again, only the starboard rotors are shown for brevity. Thrust for the front rotor, R1, was not significantly affected by configuration. However, thrust for the back rotor, R3, was greatly affected, with the *dz/R*=0.33 yielding the highest thrust, *dz/R*=0.57 coming in second, and *dz/R*=0 coming in far below. Subplots c and d show the configuration did not greatly affect torque for R3, as they all yielded similar values. This indicates that the dz/R=0 configuration was very inefficient compared to the others, since it yielded much less thrust for about the same torque, and that the *dz/R*=0.33 was the most efficient for R3. R1 had slightly higher torque values for *dz/R*=0.33, then *dz/R*=0, and finally *dz/R*=0.57 being the lowest. Thus, the *dz/R*=0.33 configuration may be slightly less efficient for the front rotors, but it is significantly more efficient for the back rotors.

Figure 15, shows the same conditions as Figure 14, but at a higher tunnel dynamic pressure of 1.90 psf. Some of the same trends are observed, mainly that the back rotor is significantly less efficient for the *dz/R*=0 configuration. Figure 15 (d) shows that the *dz/R*=0 case for the back rotor yields significantly higher torque than the other configurations for all pitch angles for higher RPM. Another difference from the lower tunnel speed condition is that the back rotor, R3, yields similar thrust values for the *dz/R*=0.33 and the *dz/R*=0.57 configurations. Additionally, the *dz/R*=0.33 and 0.57 configurations yield similar torque values at –10 deg and then branch out as pitch gets closer to 0 deg, with *dz/R*=0.33 coming in slightly higher than 0.57 for both the 2000 and 3000 RPM cases (plots c and d).

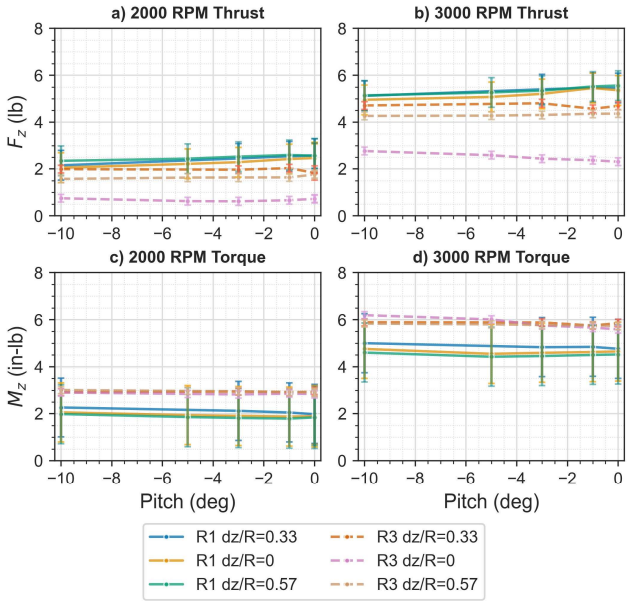

Figure 14: Starboard rotors *dz/R* comparison for thrust and torque for quadrotor configuration at *q*=0.48 psf, RPM=2000 and 3000, and tilt=0 deg.

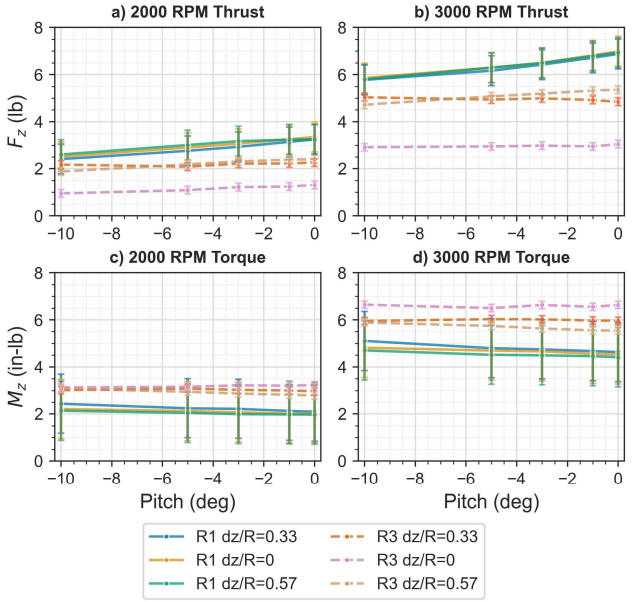

Figure 15: Starboard rotors *dz/R* comparison for thrust and torque for quadrotor configuration at *q*=1.90 psf, RPM=2000 and 3000, and tilt=0 deg.

Figure 16 shows a similar case to that in the previous figure but for the tandem configuration instead of the quadrotor configuration. The differences between the *dz/R* configurations are less pronounced for the tandem than for the quadrotor case, meaning the curves shown in Figure 16 (tandem) are closer to each other than in Figure 15 (quadrotor). Additionally, some of the trends for the torque

values in the tandem configuration are different than those for the quadrotor configuration.

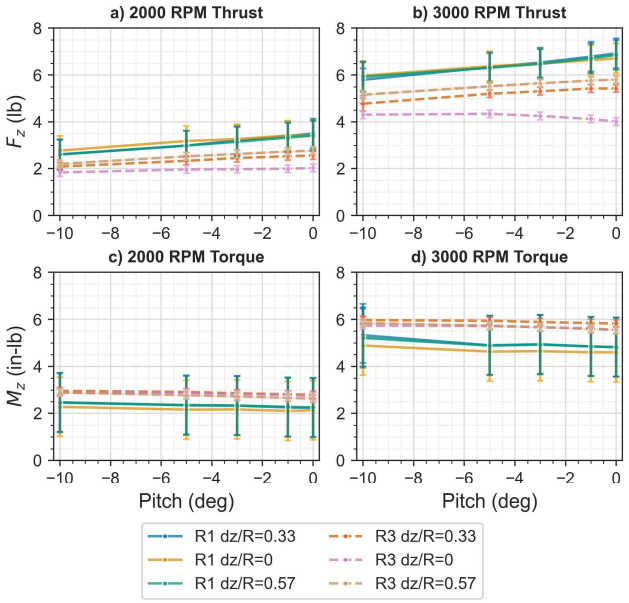

Figure 16: Starboard rotors *dz/R* comparison for thrust and torque for tandem configuration at *q*=1.90 psf, RPM=2000 and 3000, and tilt=0 deg.

The front rotor torque values are lower for *dz/R*=0 than for the other configurations for both RPMs for the tandem case, whereas for the quadrotor case, *dz/R*=0.57 was the lowest. Also, for the tandem case, the *dz/R*=0.33 torque for the back rotor, R3, is higher than for the other cases, which is also different from the trends observed in the quadrotor configuration. Previously, for the quadrotor case, R3 torque was highest for *dz/R*=0. This suggests that the configuration trends for varying rotor height may be different between the front and back rotors for a quadrotor versus a tandem. It is likely that the aerodynamic interactions from R2 and R4 in the quadrotor configuration affect the performance and characteristics of R1 and R3.

Figure 17 shows the trends between 0 and –90 deg phase for the tandem configuration for 3000 RPM at different tunnel speeds. Figure 18 shows a schematic of the quadrotor configuration with R2 and R3 phased with –90 deg separation, with the dark blue line showing blade 1 in the phased position. Note that "R1: -90 deg phase" refers to the configuration for which R3 is phased -90 deg with respect to R1 where R1 is still in the 0 deg phase position. "R1: 0 deg phase" refers to the configuration in which all the rotors are phased with 0 deg separation. The thrust values for the rotors in the 0 deg phase configuration yielded slightly higher thrust values for lower tunnel speeds for both rotors, but that difference decreased as tunnel speed increased, with similar thrust values at different phase angles. However, the back rotor, R3, still yielded slightly higher thrust for the 0 deg phase configuration. For both tunnel speeds, the torque values were higher for both the front and back rotor for 0 deg phase. The torque values themselves, as well as the difference between them, did not change much as tunnel speed was increased. The –90 deg phase configuration appears to be slightly more efficient at higher tunnel speeds for the tandem rotor case.

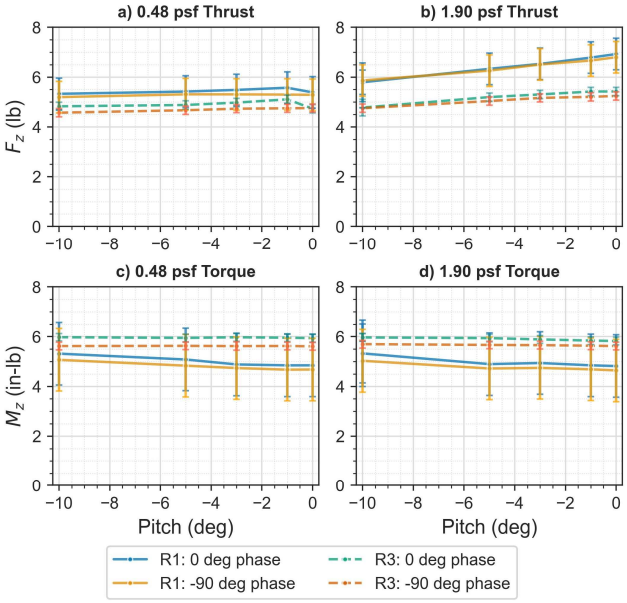

Figure 17: Starboard rotors phase comparison for thrust and torque or tandem configuration at *dz/R*=0.33, *q* = 0.48 psf and 1.90 psf, RPM=3000, and tilt=0 deg.

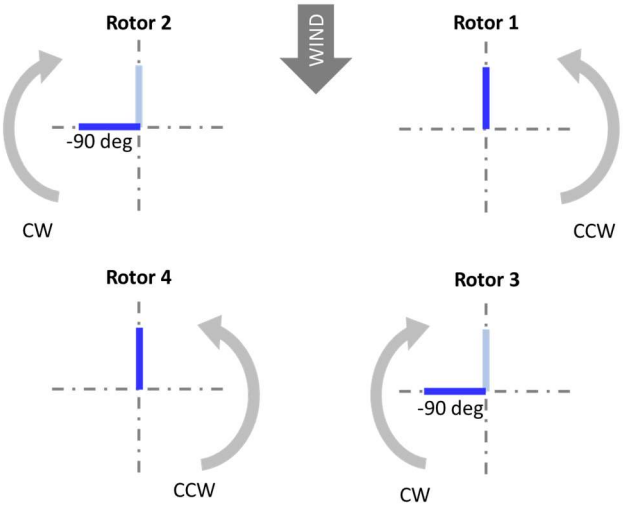

Figure 18: Schematic of rotors phased with –90 deg separation for R2 and R3 with respect to R1 and R4.

Figure 19 shows the phase comparison of thrust for each rotor in the quadrotor configuration for dynamic pressure (tunnel speed) 1.90 psf and 3000 RPM. Figure 20 and Figure 21 show schematics of the rotors phased with –30 and –60 deg separation for R2 and R3. There is not a very significant difference in the rotor thrust for the different phase values; however, for all the rotors, –90 deg phase yielded slightly lower thrust for pitch angle of –10. For the back rotors, the 0 deg phase thrust values were higher also for the -10 deg pitch angle.

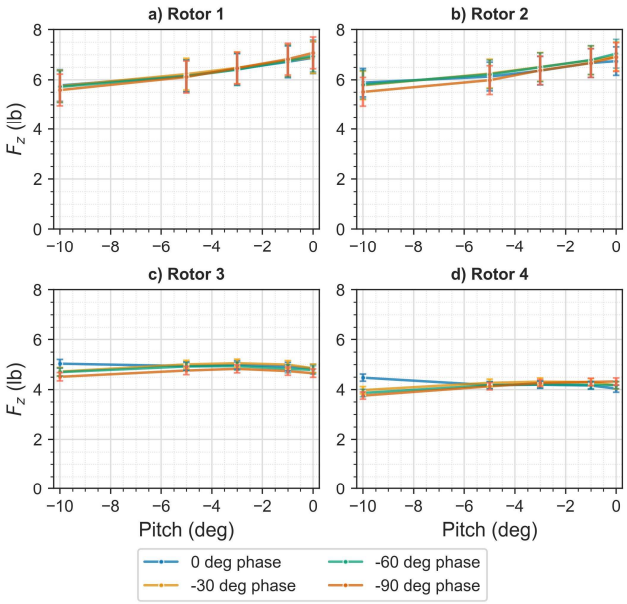

Figure 19: Phase comparison for individual thrust for quadrotor configuration at *dz/R*=0.33, *q*=1.90 psf, RPM=3000, and tilt=0 deg.

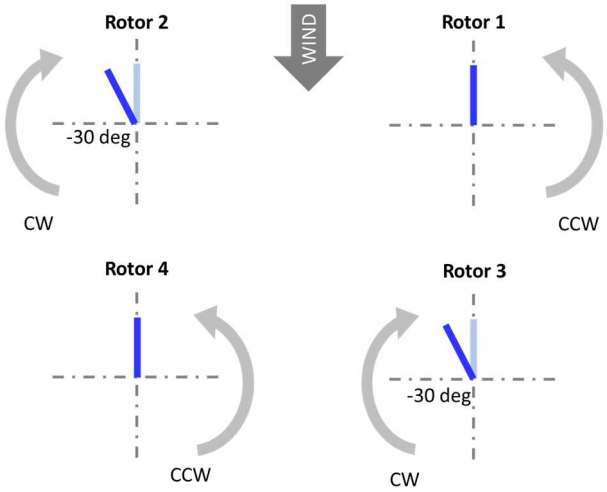

Figure 20: Schematic of rotors phased with –30 deg separation for R2 and R3 with respect to R1 and R4.

Figure 22 shows plots of the total thrust from all four rotors for the same configurations and conditions given in the previous plot. When all the thrust values are added together, both RPM cases show that the 0 deg phase case yields higher total thrust for –10 deg pitch. Additionally, at –10 deg pitch, the –90 deg phase yields the lowest thrust. When the pitch goes to 0 deg, this trend reverses and –90 deg phase yields the highest thrust and 0 deg phase yields the lowest, but the differences are much smaller.

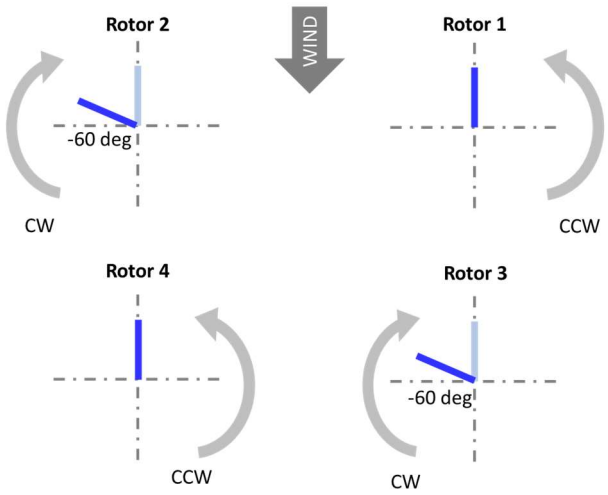

Figure 21: Schematic of rotors phased with –60 deg separation for R2 and R3 with respect to R1 and R4.

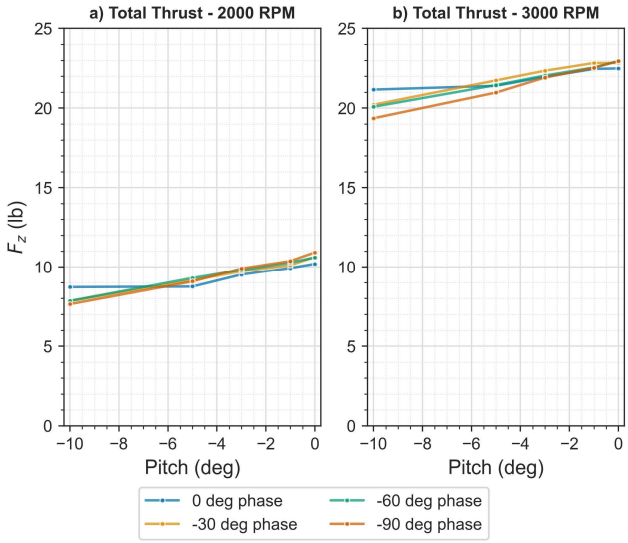

Figure 22: Phase comparison for total thrust for quadrotor configuration at *dz/R*=0.33, *q*=1.90 psf, RPM=2000 and 3000, and tilt=0 deg.

Figure 23 shows the power for the same conditions as given in the previous two figures: quadrotor, *dz/R*=0.33, *q*=1.90 psf. The –90 deg phase has the lowest power for both RPMs and all pitch angles. The differences in power are much harder to see at 2000 RPM. At 3000 RPM the 0 deg and –30 deg phase yield similar power with –60 deg coming in slightly less and –90 deg yielding the lowest. The –90 deg phase may be slightly more efficient between –5 and 0 deg pitch.

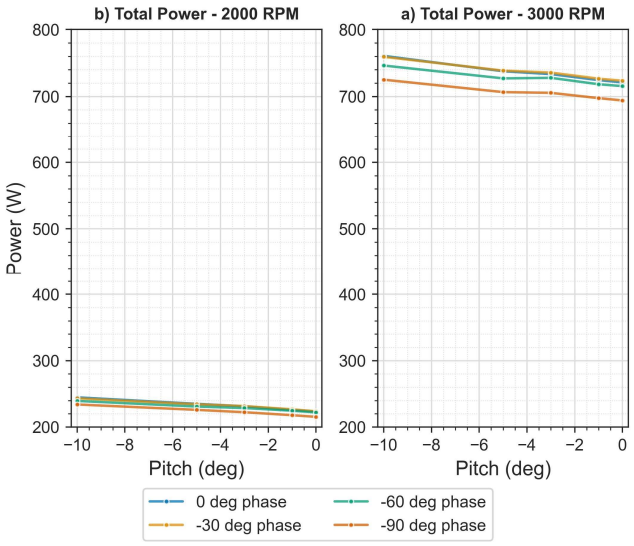

Figure 23: Phase comparison for total power for the quadrotor configuration at *dz/R*=0.33, *q*=1.90 psf, RPM=2000 and 3000, and tilt=0 deg.

Dynamic Data Results

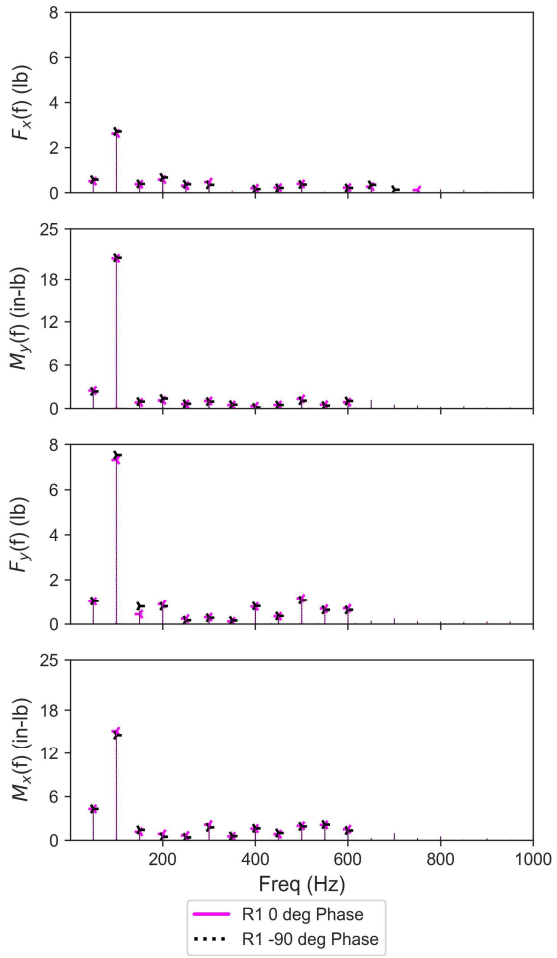

Figure 24: Dynamic plot – Tandem configuration, phase comparison for rotor 1 at *dz/R*=0, *q*=1.90 psf, RPM=3000, pitch=0 deg, and tilt=0 deg.

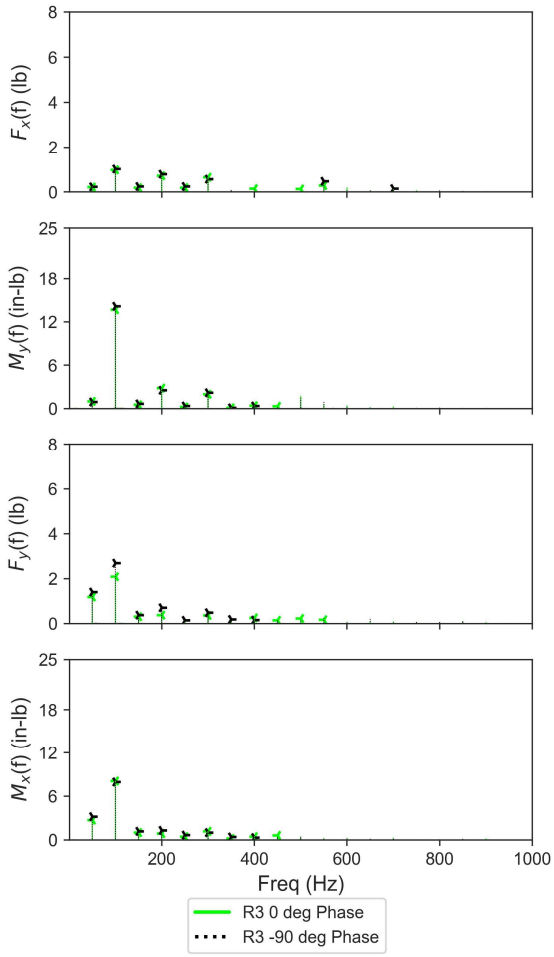

Figure 25: Dynamic plot – Tandem configuration, phase comparison for rotor 3 at *dz/R*=0, *q*=1.90 psf, RPM=3000, pitch=0 deg, and tilt=0 deg.

The plots presented in this section show the dynamic data for F_x, M_y, F_y, and M_x as functions of frequency. Each plot shows the 0 deg and –90 deg phase as a solid and dotted line, respectively. Only R1 and R3 from the quadrotor runs are shown for brevity. R1 is shown in magenta and R3 is shown in bright green. Note that all plots are for 3000 RPM; thus, the 1/rev frequency is 50 Hz, the 2/rev frequency is 100 Hz, etc.

Figure 24 and Figure 25 show dynamic data results for R1 and R3, respectively, for 0 deg and –90 deg phase for the tandem configuration for $dz/R = 0$ at 1.90 psf, 3000 RPM, 0 deg pitch, and 0 deg tilt. For all forces and moments shown, the 2/rev harmonic content is significantly lower for R3 than for R1. Additionally, for all loads, for both rotor phase angles, the 2/rev signal is significantly higher than any other signal. This is to be expected; generally, for a rotor in forward flight, the dominant harmonic is the N/rev, where N is the number of rotor blades per rotor (in this case, 2). For this tandem case, the phasing of the rotors does not have a very large impact on the harmonic content of the individual rotor loads/moments.

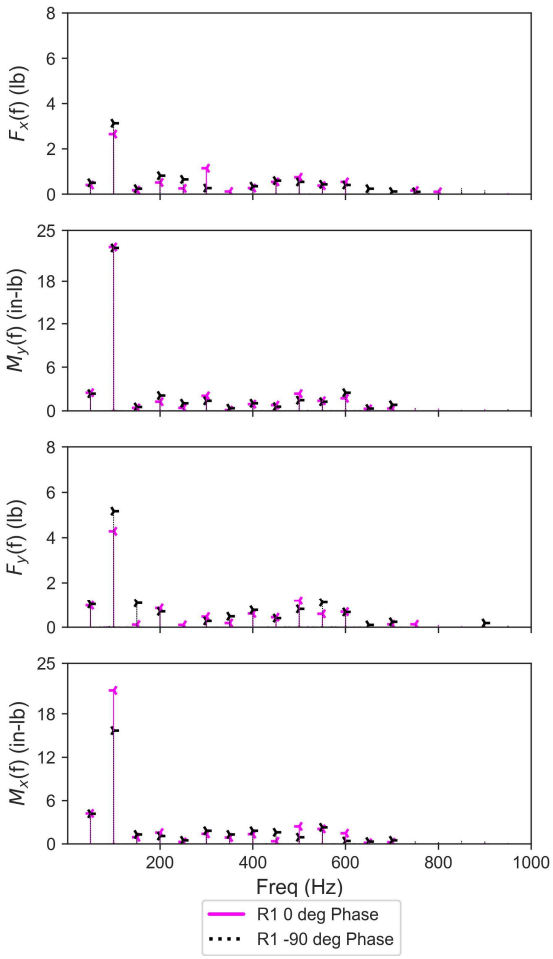

Figure 26: Dynamic plot – Quadrotor configuration, phase comparison for rotor 1 at *dz/R*=0, *q*=1.90 psf, RPM=3000, pitch=0 deg, and tilt=0 deg.

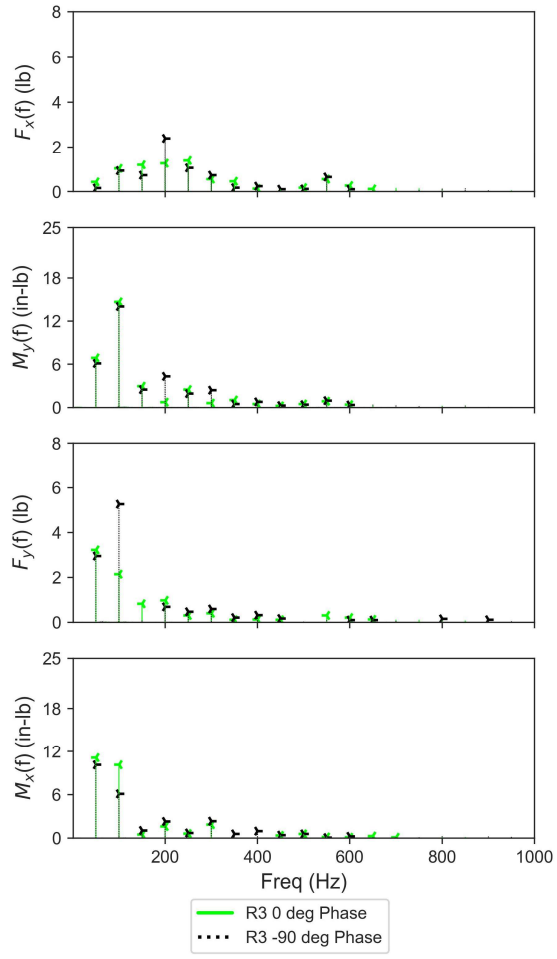

Figure 27: Dynamic plot – Quadrotor configuration, phase comparison for rotor 3 at *dz/R*=0, *q*=1.90 psf, RPM=3000, pitch=0 deg, and tilt=0 deg.

Figure 26 and Figure 27 show the same conditions as the previous two figures (Figure 24 and Figure 25), but for the quadrotor configuration. Thus, the previous two figures can be compared to Figures Figure 26 and Figure 27 to assess differences between the tandem and quadrotor configurations for dz/R=0. Like for the tandem configuration, the 2/rev signal for the front rotor, R1, in the quadrotor configuration, is significantly higher than the other signals. This trend does not hold for the back rotor in the quadrotor configuration, where other harmonics sometimes were the most significant, depending on specific load and phase condition. This inconsistency could be due to the more chaotic aerodynamic environment experienced by the back rotors. Additionally, the 2/rev signal for R1 F_y is higher for tandem than for quadrotor. R1 and R3 also show more higher frequency signals for the quadrotor configuration than for the tandem, particularly for F_x. For -90 deg phase, the 4/rev R3 F_x signal of the quadrotor was more than double that of the tandem.

Focusing on Figure 26 and Figure 27, for R3 F_x, the 4/rev frequency is nearly doubled by phasing the rotor –90 deg; however, this phasing reduces the signals of other harmonics, such as the 3/rev and 5/rev. For F_y, there are some notable dissimilarities between the front and back rotors (R1 and R3). With –90 deg phase, the 2/rev of both rotors is approximately the same. 0 deg phasing causes a significant decrease in the 2/rev F_y for the back rotor, but this reduction is not as dramatic for the front rotor. Additionally, the front rotor has significant 3/rev F_y for –90 deg phase, but none for 0 deg phase. The opposite is true for the back rotor.

Figures Figure 28 and Figure 29 show similar results to those of the previous figures, but for a front to back rotor separation of dz/R=0.33 in the quadrotor configuration. Comparing the plots with dz/R=0.33 to those of the dz/R=0 quadrotor configuration, one notable observation is that for R3, the back rotor, the 1/rev M_y, F_y, and M_x signals are significantly lower for the dz/R=0.33 configuration.

Similar to other cases, for dz/R=0.33, for a given phase, the 2/rev signals are higher for the front rotor than for the back. This may be due to differences in the aerodynamic operating environments of the front and back rotors, with the front rotor encountering relatively undisturbed air compared to that encountered by the back rotor. The air going into the back rotors may have a slight downward trajectory, affecting the vibrations seen by the back rotors.

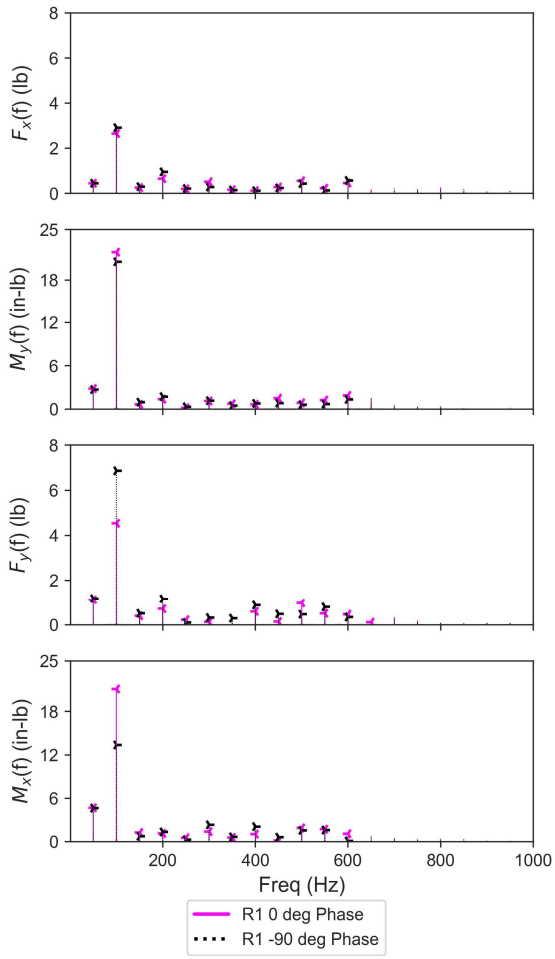

Figure 28: Dynamic plot – Quadrotor configuration, phase comparison for rotor 1 at *dz/R*=0.33, *q*=1.90 psf, RPM=3000, pitch=0 deg, and tilt=0 deg.

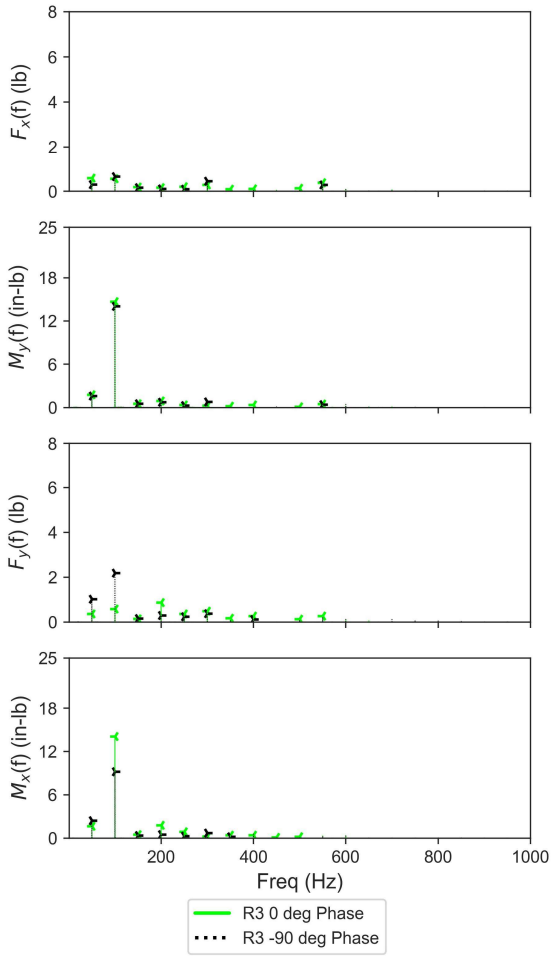

Figure 29: Dynamic plot – Quadrotor configuration, phase comparison for rotor 3 at *dz/R*=0.33, *q*=1.90 psf, RPM=3000, pitch=0 deg, and tilt=0 deg.

An additional observation is that the 2/rev F_x and M_y are relatively unaffected by the rotor phasing, for both R1 and R3. This is not the case for the 2/rev F_y and M_x, where a significant dependence on rotor phase is observed for both rotors, with the 2/rev F_y significantly increased by applying –90 deg phasing and the corresponding 2/rev M_x values significantly decreased by applying that same –90 deg phasing.

CONCLUSIONS

The Multirotor Test Bed Entry 2 (MTB2) wind tunnel test, conducted in August 2022, was summarized and described. The main focus for the MTB2 test was obtaining forces and moments for the quadrotor configuration for back rotor heights of dz/R=0, 0.33, and 0.57, where dz/R=0.33 represented the RVLT conceptual quadrotor. Additionally, this test allowed for rotor phasing and solidity studies for 2-, 3-, and 6-bladed rotors. Quasi-steady and dynamic data from the MTB2 wind tunnel test were presented and discussed. Some of the discrepancies observed in the data are as follows:

- The single rotor runs and the runs associated with the uncertainty analysis showed that the back rotors yielded lower thrust for the same conditions, potentially due to a load cell discrepancy.
- The CW spinning rotors yielded higher torque values than the CCW spinning rotors, likely due to a load cell or motor discrepancy.
- There could be a slight deviation in measurement from rotor to rotor (independent of the load cell)

(observed between front starboard rotor (R1) and the back port rotor (R4)), potentially due to slight deviations in rotor geometry.

Some of the results observed in the quasi-steady data are as follows:

- Blade loading was the highest for 2-bladed, then 3-bladed, and then 6-bladed rotors.
- The influence of tilt on thrust and torque was more pronounced at higher tunnel speeds.
- For the quadrotor configuration at both low and high tunnel speeds and RPMs, the back rotors were less efficient for dz/R=0 (front and back rotors at the same height), yielding low thrust and high torque values.
- The 0 deg phase separation configuration yielded higher thrust values for the back rotors at –10 deg pitch, compared to those of the other phase separation angles.
- Total power was higher for 0 and –30 deg phase separation and lowest for –90 deg separation for all pitch angles. The power difference between the phase separation angles increased with higher RPM.

Some of the results observed in the dynamic data are as follows:

- The quadrotor configuration yielded more high frequency content compared to the tandem configuration, likely due to more rotor-rotor aerodynamic interactions.
- For the quadrotor configuration, the 1/rev signals for the back starboard rotor (R3) M_y (pitch), F_y (side force), and M_x (roll) were significantly lower for the dz/R=0.33 configuration than for the dz/R=0 configuration.
- The rotor phasing did not significantly impact the dynamic loads for the tandem case dz/R =0.
- Rotor phasing could significantly impact both the dz/R=0 and 0.33 quadrotor configurations, for example F_y for R1 and R3, the front and back starboard rotors.

Future work for the MTB will include MTB3, tentatively scheduled for early 2026 in the NFAC. MTB3 will feature new load cells, a hub with ground adjustable collective, and a vibration damper in the rotor stack. For this next test, both acoustic and performance data will be acquired.

ACKNOWLEDGMENTS

The authors would like to acknowledge all of the members of the MTB2 Wind Tunnel Test Team and the U.S. Army 7-by 10-Foot Wind Tunnel Crew. This paper would not be possible without the post-test load cell calibration team including Isabelle Pichay and Alex Sheikman. Thank you to Gina Willink, Lead of the Ames Aeromechanics Mechanical Systems Team, for helping with the design process of the MTB. The NASA Machine Shop Team, led by Robert Kornienko and Vincent Derilo, machined the parts of the MTB and provided guidance and helpful suggestions during the design process. And as always thank you to William Warmbrodt for his outstanding leadership and to Tom Norman for invaluable guidance and assistance. Thank you to the reviewers of this work, Lauren Weist, Dorcas Kaweesa, and Sesi Kottapalli. A more complete list of acknowledgements of all individuals who helped in acquiring the MTB2 data is given in the data report [Ref. 13].

REFERENCES

1. Conley, S. and Russell, C., “Mechanical Design of the Multirotor Test Bed," VFS Aeromechanics for Advanced Vertical Flight Technical Meeting, San Jose, CA, January 21–23, 2020.
2. Russell, C. and Conley, S. "The Multirotor Test Bed – A New NASA Test Capability for Advanced VTOL Rotorcraft Configurations," VFS 76th Annual Forum & Technology Display, Virtual, October 6–8, 2020.
3. Conley, S., Russell, C., Kallstrom, K., Koning, W., and Romander, E., "Comparing RotCFD Predictions of the Multirotor Test Bed with Experimental Results," VFS 76th Annual Forum & Technology Display, Virtual, October 6–8, 2020.
4. Shirazi, D., "Comparison of the CHARM Predictions of the Multirotor Test Bed with Wind Tunnel Experimental Results," VFS Aeromechanics for Advanced Vertical Flight Technical Meeting, San Jose, CA, January 25–27, 2022.
5. Johnson, W., “Technology Drivers in the Development of CAMRAD II,” American Helicopter Society Aeromechanics Specials Meeting, January 1994.
6. Sekula, M., K., Russell, C., R., "Time-Frequency Analysis of Experimental and Analytical Hub Loads of a Rotor Undergoing a Rotor Speed Change," Vertical Flight Society 78th Annual Forum & Technology Display, Ft. Worth, TX, May 10–12, 2022.
7. Ahmad, J., “Application of Rotor Disk Model in the OVERFLOW CFD Code,” NASA/TM—20220005496, April 2022.
8. Silva, C., Johnson, W., Solis, E., Patterson, M., and Antcliff, K., “VTOL Urban Air Mobility Concept Vehicles for Technology Development,” AIAA 2018 Aviation Forum, Atlanta, GA, June 25–29, 2018.
9. Silva, C., "Updates to NASA Urban Air Mobility Reference Vehicles," Vertical Flight Society Sixth Decennial Aeromechanics Specialists' Conference, Santa Clara, CA, February 2024.
10. Kopyt, N., Niemiec, R., Gandhi, F., “Quadcopter Rotor Phasing for Minimization of Aircraft Vibratory Loads,” VFS Aeromechanics for Advanced Vertical Flight Technical Meeting, San Jose, CA, January 21–23, 2020.

11. Conley, S., “Multirotor Test Bed Load and Stress Analysis," NASA/TM-20230000313, February 2023.
12. Shirazi, D., et al, "Leveraging Modeling and Sensitivity Studies for Improving Aerodynamic Predictions for Multirotor Aircraft," To be presented at the VFS 81st Annual Forum & Technology Display, Virginia Beach, VA, May 20–22, 2025.
13. Conley, S., et al, “Multirotor Test Bed Wind Tunnel Test Data Report: Second Tunnel Entry Test Results,” NASA/TM in progress, to be published in 2025.
14. Ventura Diaz, P. and Yoon, S., “Computational Study of NASA’s Quadrotor Urban Air Taxi Concept,” AIAA SciTech Forum, Orlando, FL, January 6–10, 2020.
15. Silva, C. and Johnson, W., “Practical Conceptual Design of Quieter Urban VTOL Aircraft,” VFS 77th Annual Forum & Technology Display, Virtual, May 10-14, 2021.
16. Selig, M., *Summary of Low Speed Airfoil Data.* No. V. 1 in Summary of Low Speed Airfoil Data, SoarTech Publications, 1995.
17. Schatzman, D., “Tunnel Survey and Calibration Report - 7- x 10-ft Wind Tunnel,” U.S. Army Technical Report, A215-00-R0006, Moffett Field, CA, 2019.